Multiband Omnidirectional Ventilated Acoustic Barriers Based on Localized Acoustic Rainbow Trapping

Hong-Wei Wu[1,2,*] Yun-Qiao Yin,[1] Zong-Qiang Sheng,[1] Yang Li,[1] Dong-Xiang Qi,[2] and Ru-Wen Peng[2]

[1] *School of Mechanics and Photoelectric Physics, Anhui University of Science and Technology, Huainan 232001, China*
[2] *National Laboratory of Solid State Microstructures, School of Physics, and Collaborative Innovation Center of Advanced Microstructures, Nanjing University, Nanjing 210093, China*

In this paper, we propose a subwavelength closed surface consisting of radial gradient grooves for achieving localized acoustic rainbow trapping. Similar to conventional rainbow trapping based on a plane structured surface, we demonstrate that rainbow trapping can also be realized by a closed surface in the deep-subwavelength scale. In particular, the trapped spatial positions on the closed surface can be freely tuned by changing the structural parameters. Based on the advantages of the multiband response and subwavelength dimension of this structure, we propose an acoustic barrier consisting of an array of closed surfaces to achieve multiband sound insulation and high ventilation simultaneously. Investigated results indicate that this kind of acoustic barrier possesses the features of subwavelength scale, and multiband and omnidirectional responses for blocking incident acoustic waves, yet has high ventilation. Finally, we discuss the influence of the channel width on the magnitude and bandwidth of the transmission loss spectrum. The experimental results agree with our theoretical prediction that the material losses can broaden the response bandwidth, and form broadband sound insulation. The acoustic barrier consisting of localized rainbow trapping structures may have many applications in infrastructure requiring air-permeability and sound-proofing.

I. INTRODUCTION

Acoustic rainbow trapping is highly desirable in various scenarios ranging from enhanced acoustic sensing, and acoustic signal processing and filtering to broadband sound absorption, with the advantages that the sound wave can be freely modulated and broadband trapped at particular positions. In fact, the concept of rainbow trapping was initially proposed from studies in quantum optics and nonlinear optics to overcome the constraint between high optical delay and broad bandwidth [1–3]. In classical optical systems, with the development of artificial microstructures and metamaterials, optical rainbow trapping and slow-light devices have been realized by using gradient plasmonic grating structures [3], self-similar coaxial waveguides [4], insulator-metal-insulator waveguides [5], and metal-insulator-metal waveguide tapers [6]. Furthermore, patterned hyperbolic metamaterial waveguide taper arrays consisting of multilayered metal-dielectric thin films have been proposed to realize large-area rainbow trapping with broadband absorption [7]. Generally, materials with strong

dispersion are required to achieve rainbow trapping. However, in the acoustic counterpart, the lack of strong dispersion for sound in natural materials makes it more difficult to realize rainbow trapping.

With the development of phononic crystals, and acoustic metamaterials and metasurfaces, a class of promising artificially structured materials has filled in the gap of natural materials to realize strong acoustic dispersion [8–11]. To demonstrate acoustic rainbow trapping, many structured materials have been proposed to achieve this effect, including phoxonic waveguides with holes drilled on silicon membranes [8], periodically grooved rigid metawires [9], an array of gradient grooves perforated on a rigid panel [10], and anisotropic acoustic structures [11]. Furthermore, the textured metasurface with space coiling [12] and an array of artificial Mie resonators have also been proposed to realize rainbow trapping for better utilization of space [13]. However, the aforementioned rainbow trapping devices are almost one-dimensional plane structures. In fact, miniaturization and integration are highly desirable in the developing trends of acoustic devices. Therefore, it will naturally be asked if the acoustic rainbow trapping effect can also be achieved by a closed surface on the subwavelength scale.

---

*hwwu@aust.edu.cn

054033-1

Moreover, it is a persistent pursuit for simultaneous noise attenuation and ventilation in several places, such as buildings, heavy machinery cabins, and stations. However, designing conventional acoustic barriers has always required a trade-off between sound-insulating efficiency and ventilating capabilities [14–16]. Recently, the development of acoustic metasurfaces has offered the possibility of designing acoustic barriers with efficient sound insulation and ventilation simultaneously [17]. Following this, various localized resonant units have been proposed, such as Helmholtz resonators [18], membranes [19,20], coiled spaces [21,22], etc. In these efforts, the mechanisms of local resonance or Fano-like interference for sound insulation inevitably led to a narrow working frequency range [23–26]. However, it is well known that noise usually covers a wide frequency and angle range, and it is important that this is considered when designing a broadband, or at least multiband, omnidirectional acoustic ventilation barrier. Recently, some efforts have been made to broaden the working frequency and incident-angle range based on different physical mechanisms, including double-layered perforated metastructures based on acoustic absorbers with multifrequency resonances [27], hornlike helical metasurfaces based on the superpositions between monopolar and dipolar resonant modes [28], and hooklike metasurfaces in acoustic waveguides [29], etc.

In this paper, we firstly propose a theoretical model to realize the acoustic rainbow trapping effect in a localized structure based on a subwavelength closed surface sculpted with radial gradient grooves. By means of the homogenization metamaterial approximation, we analytically derive the dispersion relations, stopped stations, field enhancement factors, and spatial field distributions of the spoof acoustic surface waves (SASWs) propagating along the azimuthal direction of the structure. It is important that the trapped positions of the SASWs can be freely tuned by tailoring the structured gradient and initial inner radius. Taking into account the advantages of multiband responses and subwavelength scale in the localized rainbow trapping structure, we design an acoustic barrier that possesses multiband, omnidirectional sound insulation, and high ventilation. Simulated results indicate that the acoustic barrier can still block 90% of incident energy even when considering the viscous and thermal losses at multiple frequencies, and keep 60% of the air flow. Moreover, to demonstrate the wide-angle response of the acoustic barrier, we also calculate the transmission losses for different incident angles and frequencies, and find that the multiband blocking efficiency remains almost unchanged from 0° to 180°. Finally, we also discuss the influence of the channel width on the bandwidth of sound insulation, and the results indicate that broadband sound insulation can be achieved by increasing the channel width. Furthermore, we conduct experimental measurements and the results indicate that the material losses effectively

broaden the response frequency of sound insulation. This kind of acoustic barrier based on the localized acoustic rainbow effect may open a route to designing sound insulators that meet the requirements of broadband response, subwavelength scale, omnidirectional blocking, and high ventilation.

II. THEORICAL MODEL OF LOCALIZED ACOUSTIC RAINBOW TRAPPING

Acoustic rainbow trapping is a phenomenon of strong acoustic dispersion, which allows spatial-spectral modulation and broadband sound trapping. It has been widely investigated based on plane rigid surfaces sculpted with gradient grooves [10,12]. This kind of acoustic rainbow trapping, in which the SASWs with different frequencies propagating along the plane surface are trapped into target grooves at different positions, is referred to as propagating acoustic rainbow trapping. In this paper, we demonstrate that the acoustic rainbow trapping effect can also be supported on a subwavelength closed surface, in which case it is referred to as localized acoustic rainbow trapping. Figure 1(a) schematically shows the closed surface sculpted with gradient grooves. Here, we consider the two-dimensional (2D) scenario, i.e., the cylinder is infinitely long along the z direction. The pressure field distribution under the structure in Fig. 1(a) vividly indicates that the incident waves are coupled to the structure from the right hand side (as shown by the orange arrow) to form SASWs traveling along the closed surface clockwise and anticlockwise simultaneously. Once the frequency of the traveling surface wave exceeds the cutoff frequency of a certain groove, then the surface wave will be trapped and stops at the groove; this feature is similar to propagating rainbow trapping in the
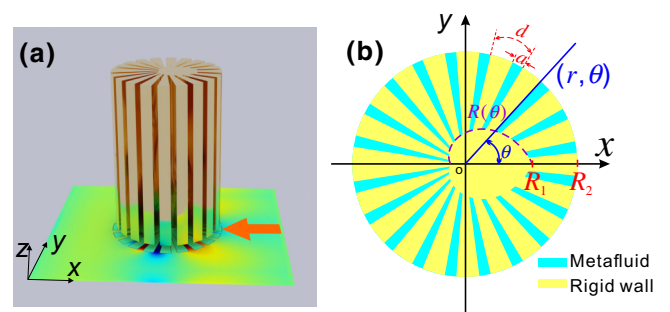

FIG. 1. (a) Schematic diagram of closed surface decorated with gradient grooves. The pressure field distribution under the structure indicates the trapped feature. The orange arrow indicates the direction of incident waves. (b) Two-dimensional structure with outside radius R_2, initial inner radius R_1, period d, and groove width a. The groove's base (variable inner radius) is defined by $R(\theta) = R_1 \exp(-\alpha\theta)$, where α is gradient factor. Yellow regions are rigid material, and cyan regions represent metafluid.

plane structured surface [10]. It is well known that the entire structure is difficult to attain at the subwavelength scale with radial grooves filled only with air. Generally, the grooves can be designed as zigzag channels or spiral channels to increase the length of the grooves to realize the subwavelength scale [21,30]. Here, as a theoretical model, the long grooves filled with air can be considered equivalent to short grooves filled with an anisotropic metafluid; the detail is shown in the Supplemental Material [31]. Thus, Fig. 1(b) shows the 2D structure for the grooves filled with a metafluid, where cyan represents the metafluid and yellow represents the rigid wall. The period and groove width are represented by d and a, and (r, θ) are the polar coordinates. The outside radius is R_2, while the inner radius is a variable $R(\theta) = R_1 \exp(-\alpha\theta)$ with azimuthal angle θ. Here R_1 is the initial inner radius corresponding to $\theta = 0°$ and α is the gradient factor. Thus, the groove's geometrical length is a gradient variable dependent on the azimuthal angle as $h(\theta) = R_2 - R_1 \exp(-\alpha\theta)$, while the wave path of the metafluid in the grooves is $H(\theta) = mh(\theta) = m[R_2 - R_1 \exp(-\alpha\theta)]$, where m is the effective refractive index of the metafluid (corresponding to a compression factor of the groove length as illustrated in Note 1 of the Supplemental Material [31]). As shown in Fig. 1(b), we hypothesize that the SASWs with different frequencies propagate along the upper and lower surfaces and are gradually trapped by the grooves with different depths before the SASWs reach the deepest groove. Thus, the two SASWs will not propagate across whole surface to form resonant modes. This hypothesis is reasonable when the frequency of the SASW is higher than the cutoff frequency of the deepest groove. Based on this hypothesis and the homogenized metamaterial approximation [32] (details are presented in the Supplemental Material [31]), we can write the pressure field distributions in different regions as

$$P_{\mathrm{I}} = A e^{-\tau(r-R_2)} e^{-i\beta R_2\theta}, \tag{1}$$

for region I ($r > R_2$, $0 < \theta < 180°$), and

$$P_{\mathrm{II}} = [B\cos(k_0 mr) + C\sin(k_0 mr)] e^{-i\beta R_2\theta}, \tag{2}$$

for region II [$R(\theta) < r < R_2$, $0 < \theta < 180°$]. It is worth noting that the structure is symmetric about the x axis, thus we only consider the upper half of the structure. In Eqs. (1) and (2), A, B, and C are the amplitude coefficients, k_0 is the incident wave number with $k_0^2 = \tau^2 + \beta^2$, τ is the radial wavevector component, and β is the azimuthal wavevector component, satisfying the condition $\beta > k_0$ for the SASWs propagating along the closed surface. The corresponding acoustic velocity fields in different regions can be obtained from $V_q = -(i\omega\rho_j)^{-1}\partial P_j/\partial q$ ($j =$ I, II), where $q = r$, θ. By matching the boundary conditions [pressure fields P_j and radial velocity components V_r are continuous at the interface $r = R_2$, and simultaneously the radial

velocity component V_r is forced to be 0 at the groove's base $r = R(\theta)$], we can obtain the dispersion relation as a function of azimuthal angle

$$\beta = k_0\sqrt{1 + (a/d)^2 \tan^2[k_0 H(\theta)]}, \tag{3}$$

and the corresponding group velocity distribution of the SASWs can be written as $V_g = (d\beta/d\omega)^{-1}$. These results allow us to inspect the trapped positions of SASWs on the closed surface.

Based on the aforementioned theoretical analysis, we calculate the dispersion relation as a function of azimuthal angle in Fig. 2(a). Here, the structural and material parameters are selected as initial inner radius $R_1 = 0.6R_2$, gradient factor $\alpha = 0.5$, effective refractive index of metafluid $m = 2$, volume-filling ratio of the metafluid $a/d = 2/3$, sound speed in air $c_0 = 343$ m/s, and mass density of air $\rho_0 = 1.21$ kg/m^3. It is not difficult to see that the cutoff frequency gradually decreases with increasing azimuthal angle θ [the larger azimuthal angle θ, the longer the groove depth $h(\theta)$]. For the groove depth that satisfies $h(\theta) = R_2 - R_1 \exp(-\alpha\theta)$, we know that the dispersion curves are denser in the larger azimuthal angle region.
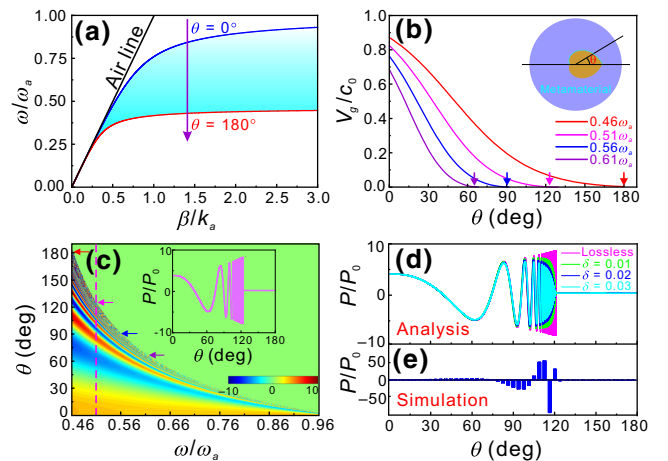

FIG. 2. (a) The dispersion curves of gradient grooves on closed surface with different azimuthal angles from $0°$ to $180°$. The black solid line represents the sound line in air. (b) Calculated group velocities of the SASWs with frequencies $\omega = 0.46\omega_a$, $\omega = 0.51\omega_a$, $\omega = 0.56\omega_a$, $\omega = 0.61\omega_a$ propagating along the metamaterial surface shown in the inset. The arrows with purple, blue, pink, and red mark the trapped positions of the SASWs with different frequencies. (c) Normalized sound pressures as a function of azimuthal angle θ and angular frequency ω along the groove's base. The four arrows marking the trapped positions are the same as those in (b). The inset shows the pressure field distribution for frequency $\omega = 0.51\omega_a$ marked by the pink vertical line. (d) Pressure field distributions along the azimuthal direction for different losses $\delta = 0$, $\delta = 0.01$, $\delta = 0.02$, $\delta = 0.03$ from analytic calculations. (e) Simulated pressure field distribution of physical structure for the grooves filled with metafluid.

The black solid line represents the sound line of air. Here, the angular frequency ω is normalized to ω_a, which corresponds to the cutoff angular frequency of the shallowest groove [groove length $h(0°) = R_2 - R_1$], and the wavevector component β along the azimuthal direction is normalized to $k_a = \omega_a/c_0$. Figure 2(b) shows the group velocities of the SASWs propagating along structural surface at different frequencies. The top right inset shows the structure based on the homogenized metamaterial approximation and marks the azimuthal angle θ. We can see that the SASWs will be stopped at different stations on the structural surface for different frequencies. The spatial-spectral separation phenomenon means that the closed surface can realize the acoustic rainbow trapping effect.

As in propagating rainbow trapping [10], the deeper grooves possess a stronger field-confinement capacity, which leads to field enhancement at the groove's base. Thus, we also calculate the pressure field distributions for different frequencies and azimuthal angles in Fig. 2(c) at the groove's base $r = R(\theta)$. In Fig. 2(c), we can see that the SASW with frequency $\omega = 0.46\omega_a$ is stopped at $\theta = 180°$, and simultaneously the pressure field is obviously enhanced. The trapped behavior is applicable for the SASWs with higher frequencies, while the field enhancement factors are decreased due to the weak field-confinement capacity of shallower grooves. As an example, the inset of Fig. 2(c) shows the slowdown of the SASW with frequency $\omega = 0.51\omega_a$ and field enhancement along the azimuthal direction. Unambiguously, the SASW is stopped at the station $\theta = 125°$, and the field enhancement factor achieves $P/P_0 = 9$. In this discussion, we do not consider the material losses. In fact, when acoustic waves propagate through channels with small dimensions, the viscous and thermal losses should be significant. Thus, we also consider the losses by adding an imaginary part δ into the effective refractive index in Fig. 2(d). The SASW propagating along the surface in the lossless case is shown with a pink line as a reference; the green, blue, and cyan lines represent the field distributions corresponding to losses $\delta = 0.01$, 0.02, and 0.03, respectively. It is easy to see that the fields are consistent at small azimuthal angles for different losses, while the pressure field is sharply decreased when the surface wave nears the trapped location for larger losses. To verify the theoretical prediction, we also carry out a numerical simulation using the acoustic module preset in COMSOL Multiphysics to calculate the pressure field distributions at the groove's base $r = R(\theta)$ as shown in Fig. 2(e). In this simulation, we set the anisotropic metafluid (material parameters are discussed in the Supplemental Material [31]) into the practical gradient grooves, the number of grooves is $N = 90$, and the structure's outside radius $R_2 = 5$ cm; other structural and material parameters are the same as the parameters used in the theoretical calculation. Due to the symmetry of the structure, we only pick up the field distribution at
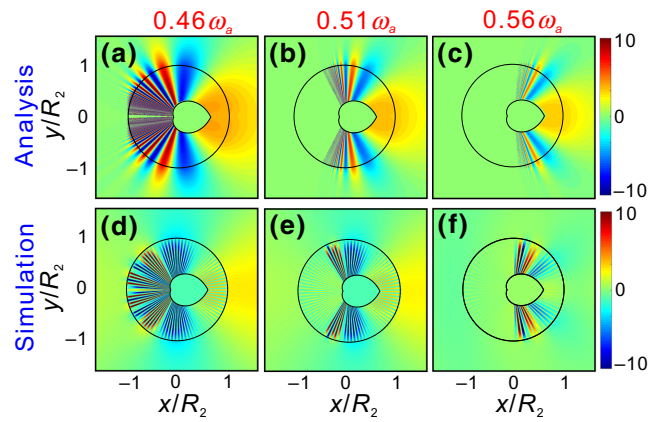

FIG. 3. Analytic calculations (a)–(c) and numerical simulations (d)–(f) of scattering pressure field distributions for different frequencies $\omega = 0.46\omega_a$, $\omega = 0.51\omega_a$, $\omega = 0.56\omega_a$.

the groove's base of the upper part (i.e., $0° < \theta < 180°$) of the structure. The length of the blue bars in Fig. 2(e) represents the field enhancement factor P/P_0, and the intervals between the blue bars indicate the rigid wall region with zero field intensity. The simulated results make clear that the stopped station and field enhancement of SASW are almost in agreement with the theoretical calculations in Fig. 2(d).

To more clearly show the spatial-spectral separation of acoustic rainbow trapping, the spatial field distributions are analytically calculated and numerically simulated for different frequencies $\omega = 0.46\omega_a$, $\omega = 0.51\omega_a$, $\omega = 0.56\omega_a$ in Fig. 3. Here, the metamaterial model is used in the analytical calculation as shown in Figs. 3(a)–3(c), while the physical structure for gradient grooves filled with metafluid is simulated as shown in Figs. 3(d)–3(f). We can see that the SASWs are stopped at different locations $\theta = 180°$, $\theta = 125°$, $\theta = 88°$ for different frequencies $\omega = 0.46\omega_a$, $\omega = 0.51\omega_a$, $\omega = 0.56\omega_a$. Obviously, the wavelengths of the SASWs become shorter and the field intensities of the SASWs become stronger when the SASWs are closer to the stopped stations. The simulated results are consistent with the analytical calculations.

At the beginning of this section, we propose a hypothesis that the SASWs propagating along the upper and lower surfaces are gradually trapped by the gradient grooves, rather than traversing the entire surface of the structure. This hypothesis is reasonable when the frequencies of the SASWs are higher than the cutoff frequency of the deepest groove located at $\theta = 180°$. If the frequency of the SASW decreases below the cutoff frequency, then the SASWs will propagate along the entire closed surface to form resonant modes. In order to confirm this conclusion, we calculate the field distributions of modes by using the acoustic module preset in COMSOL Multiphysics for different frequencies $\omega = 0.38\omega_a$, $\omega = 0.40\omega_a$, $\omega = 0.42\omega_a$, $\omega = 0.44\omega_a$ as

shown as Fig. S3 in the Supplemental Material [31]. It is not difficult to see that the modes of Figs. S3(a)–S3(d) correspond to quadrupole, hexapole, octupole, and decapole resonant modes from the inhomogeneous field distributions, respectively.

It is important to be able to freely tune the stopped stations of the SASWs by tailoring the structural parameters in many practical applications. In the discussion of Fig. 2, we see that the trapped location depends strongly on the groove depth $h(\theta) = R_2 - R_1 \exp(-\alpha\theta)$. That is to say, we can change the initial inner radius R_1 and the gradient factor α to effectively modulate the stopped station of the SASW. To show the tunability, we investigate the pressure field distribution along the groove's base $R(\theta) = R_1 \exp(-\alpha\theta)$ as indicated by the cyan curve in the inset of Fig. 4(a) for the gradient factor α changing from $\alpha = 0.5$ to 2.0. The parameters are selected as $R_1 = 0.6R_2$, $\omega = 0.46\omega_a$, $\delta = 0.01$, and other parameters are the same as previous settings. With increasing gradient factor, the grooves become steeper and lead to the stopped stations' antedisplacement. To clearly show the result, we consider the field distribution of the SASWs with frequency $\omega = 0.46\omega_a$ for $\alpha = 0.5$, 0.75, and 1.0 indicated by cyan, blue, and red curves, respectively, in Fig. 4(b). It is very obvious that the stopped station moves from $\theta = 180°$ to $\theta = 88°$ when the gradient factor α increases from 0.5 to 1.0. In Fig. 4(c), we calculate the pressure field distribution along the groove's base as indicated by the cyan curve in the inset of Fig. 4(a) as the initial inner radius is changed from $R_1 = 0.2R_2$ to

$0.8R_2$ and the gradient factor is kept at $\alpha = 0.5$. When increasing the initial inner radius R_1, the groove lengths are uniformly shortened, then the asymptotic frequencies are increased correspondingly. Thus, the stopped station of the SASW with frequency $\omega = 0.46\omega_a$ is moved to a larger azimuthal angle, as shown in Fig. 4(c). Figure 4(d) shows the field distributions corresponding to $R_1 = 0.3R_2$, $R_1 = 0.4R_2$, and $R_1 = 0.5R_2$ as cyan, blue, and red curves, respectively. The stopped stations are at $\theta = 93°$, $127°$, and $151°$ corresponding to $R_1 = 0.3R_2$, $R_1 = 0.4R_2$, and $R_1 = 0.5R_2$.

III. MULTIBAND OMNIDIRECTIONAL VENTILATED ACOUSTIC BARRIER

In the previous discussion, we achieve the localized acoustic rainbow trapping effect on a subwavelength closed surface. Owing to the distinctive features of the subwavelength scale and multiband responses of the gradient structure, it is potentially possible to design an acoustic barrier that can achieve continuous broadband omnidirectional ventilated sound insulation. Thus, in the following we design a realizable practical acoustic rainbow trapping structure to construct a one-dimensional acoustic barrier.

In order to realize the anisotropic metafluid in grooves for the subwavelength-scale structure, we design canonical zigzag channels along the radial direction on the closed surface, as shown in the left of Fig. 5(a), and the channels are distributed symmetrically on the left and right sides of the structure. The structural parameters are outside radius $R_2 = 5$ cm, inner radius $R_1 = 3.4$ cm, width of zigzag channel $a = 0.3$ cm, channel period $d = 1.57$ cm, wall thickness $t = 0.1$ cm, and the number of channels $N = 20$. The boundary of the heart-shaped area is described by $R(\theta) = R_1 \exp(-\alpha\theta)$, where the gradient factor $\alpha = 0.35$. The acoustic barrier, shown in the right of Fig. 5(a), is an array of the closed surface structures with period l, and the sound wave illuminates this barrier with angle ϕ. At the first step, we investigate the transmission loss (TL) spectrum [TL $= 10\log_{10}(p_{\text{inc}}/p_t)$, where p_{inc} and p_t are the incident and transmitted powers, respectively] for different periods l for normal incidence (i.e., the incident angle $\phi = 0°$) in Fig. 5(b). We see that there are nine TL peaks for period $l = 15$ cm present in the TL spectrum. Here, the reason for discrete TL peaks is that a small number of discrete zigzag channels with large long gradients on the surface are more likely to induce the resonances of zigzag channels with different frequencies due to weak coupling between adjacent channels. In fact, if the distance between adjacent zigzag channels is sharply decreased to generate strong coupling, the SASWs are formed and propagate along the closed gradient surface. When increasing the period l, the TL peaks are almost unmovable, except for the peak with the highest frequency. The peak with the highest frequency is sensitive to the increase in period because it is very near
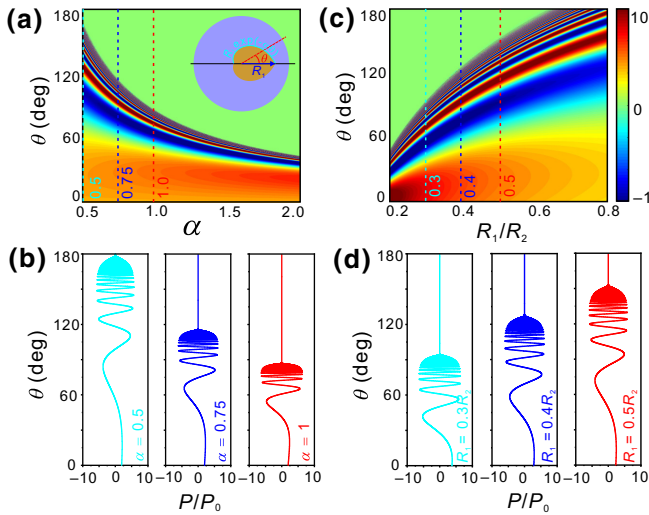

FIG. 4. (a) The pressure distributions as a function of azimuthal angle θ and gradient factor α. The cyan, blue, and red vertical lines represent gradient factors $\alpha = 0.5$, 0.75 and 1.0, and corresponding field distributions are shown in (b). (c) The sound pressure field distributions as a function of azimuthal angle θ and initial inner radius R_1. The cyan, blue, and red vertical lines represent initial inner radius $R_1 = 0.3R_2$, $0.4R_2$ and $0.5R_2$, and corresponding field distributions are shown in (d).
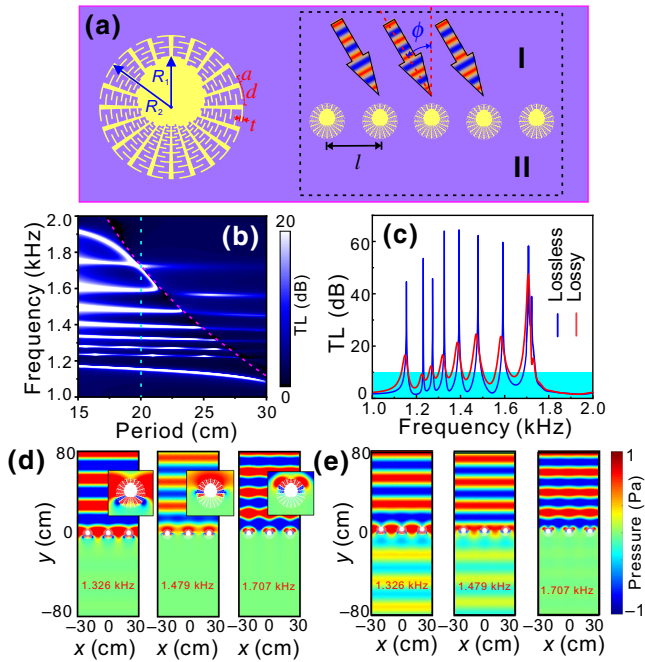
FIG. 5. (a) Left: Schematic diagram of structural unit with structural parameters: outside radius R_2, initial inner radius R_1, channel width a, channel period d, and wall thickness t. Right: acoustic barrier with period l is illuminated by plane wave with incident angle ϕ from region I, and II represents transmission zone. (b) The TL spectra as a function of frequency f and period l for incident angle $\phi = 0°$. Red dotted line corresponds to the Wood's anomalies. (c) The TL spectrum for period $l = 20$ cm marked by cyan vertical line in (b) for lossless (blue line) and lossy (red line). Cyan region indicates the 10 dB level. (d) and (e) show the pressure field distributions at different frequencies corresponding to lossless and lossy, respectively. Insets in (d) show the trapped details of gradient structure.

to the locations of the Wood's anomalies. The Wood's anomalies are a spectral anomaly phenomenon in grating diffraction for incident waves that satisfy $d(1 + \sin\phi) = n\lambda$ ($n = 1, 2, 3 \dots$), where λ is the incident wavelength [33,34]. In our acoustic barrier, the red dotted line in Fig. 5(b) indicates the locations of the Wood's anomalies.

In order to clearly observe the TL spectrum, we consider the TL spectrum of $l = 20$ cm, marked by the cyan dashed line of Fig. 5(b), in Fig. 5(c). By observing the solid blue line, we can see that all TL peaks exceed 40 dB; in other words, the acoustic barrier blocks almost all incident energy at the eight frequencies. It is worth noting that the ventilation window reaches 50% for period $l = 20$ cm. In fact, higher ventilation can be realized when further increasing the period, as shown in Fig. 5(b), while the intensities of the TL peaks still exceed 10 dB (the value TL > 10 dB means that the acoustic barrier can effectively block 90% of incident energy for multiple frequencies), as the ventilation window is 60% for period $l = 25$ cm. When acoustic waves propagate through radial channels

with small dimensions, the losses should be significant. Thus, we also consider the viscous and thermal losses in the simulation shown by the red solid line in Fig. 5(c). Notably, this condition is an approximation to the full thermoviscous solution, but it is applied in a pressure acoustics model by adding a weak contribution to implement the boundary layer impedance (BLI) condition in COMSOL Multiphysics. We can see that the TL peaks are obviously reduced at lower frequencies due to larger losses in deeper channels. However, we can still observe that all the TL peaks exceed 10 dB. Figures 5(d) and 5(e) show the pressure field distributions at the same frequencies for the incident waves irradiating from top to bottom. The left and right boundaries of the barrier are set as the Floquet periodic boundary conditions. Figure 5(d) corresponds to the lossless case, while Fig. 5(e) corresponds to the lossy case. The insets in Fig. 5(d) indicate that the SASWs with different frequencies are trapped at different stations. These field distributions presented in Figs. 5(d) and 5(e) suggest that the incident energies are effectively blocked even when considering the viscous and thermal losses in the structure. From this discussion, the results imply that the acoustic barrier based on a localized rainbow trapping structure can achieve multiband ventilated sound insulation for normal incidence.

Considering the random incident angles that the acoustic signals may have in practical noise control situations, it is important to investigate the angular dependence of transmission loss of our proposed acoustic barrier. We calculate the TL spectra of an acoustic barrier with period $l = 20$ cm for different incident angles ϕ in Fig. 6(a). The red dotted lines indicate the locations of the Wood's anomalies corresponding to $n = 1$ (bottom left) and $n = 2$ (top right). Increasing the incident angle from 0° to 90°, we can see
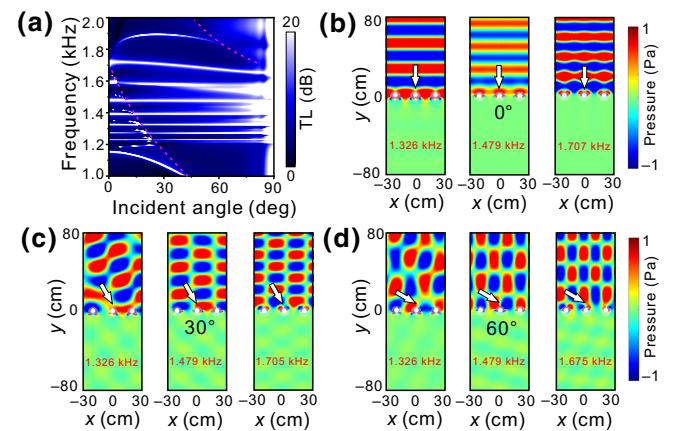

FIG. 6. (a) The TL spectra as a function of frequency and incident angle. Red dotted lines mark the locations of the Wood's anomalies. (b)–(d) show the spatial field distributions for different incident angles $\phi = 0°$, 30°, 60°. The period $l = 20$ cm, and other parameters are same as ones in Fig. 5. White arrows mark the incident directions.
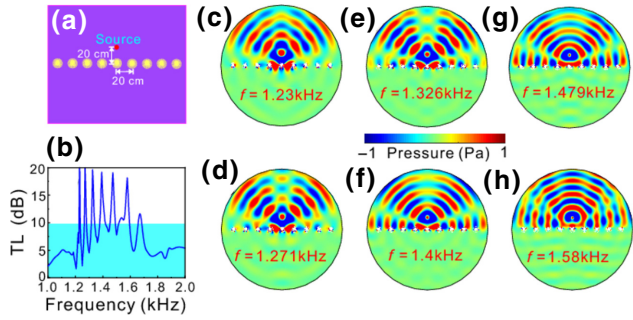
FIG. 7.   (a) Schematic diagram for a point source 20 cm above the barrier. (b) The TL spectrum for the structure illuminated by the point source. Cyan region indicates the 10 dB level. (c)–(h) show the pressure field distributions for different frequencies.
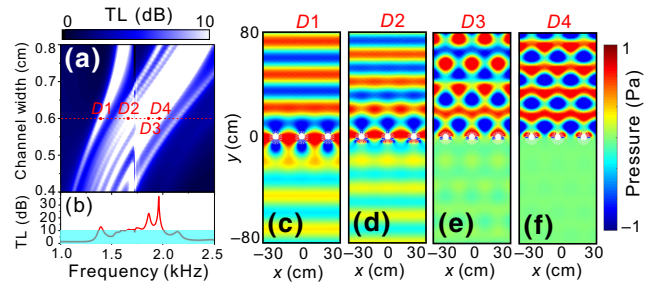

FIG. 8.   (a) The TL spectra as a function of channel width and frequency for considering the losses. The TL spectrum for channel width $a = 0.6$ cm marked by red dashed line is presented in (b). Cyan region in (b) indicates the 10 dB level. (c)–(f) show the pressure field distributions at frequencies $f = 1.395$ kHz ($D1$), 1.67 kHz ($D2$), 1.865 kHz ($D3$), and 1.96 kHz ($D4$), respectively.

that the intensities of these TL peaks throughout exceed 20 dB. Thus, the barrier has excellent blocking properties for the incident wave with incident angles from 0° to 180° due to structural symmetry. Figures 6(b)–6(d) show the simulated acoustic pressure field distributions caused by the proposed barrier when illuminated by a plane wave with incident angles $\phi = 0°$ [Fig. 6(b)], $\phi = 30°$ [Fig. 6(c)], and $\phi = 60°$ [Fig. 6(d)] for various frequencies. In the transmission region, the intensities of transmitted waves drop to almost 0 at these frequencies. In order to further verify the advantages of the omnidirectional, multiband, and ventilated acoustic barrier, we set a point source above the barrier consisting of nine structural units separated by a distance of 20 cm as shown as Fig. 7(a). Figure 7(b) shows the TL spectrum for the point source case, in which seven TL peaks exceed 10 dB. In Figs. 7(c)–7(h), the simulated acoustic pressure field distributions are presented, and we can see that the acoustic energies are almost blocked to the region above the barrier.

IV. INFLUENCE OF CHANNEL WIDTH ON THE BANDWIDTH OF SOUND INSULATION

In Fig. 5(c), we show the influence of the viscous and thermal losses on the TL spectrum. The results indicate that the losses necessarily decrease the magnitude of the TL peaks and broaden the peak width, simultaneously. In fact, the zigzag channel width of the closed surface will significantly influence the TL spectrum. More specifically, the larger channel width not only decreases the viscous and thermal losses, but also leads to broader peak width due to a lower confinement capacity for the SASWs. Thus, we now discuss the influence of the zigzag channel width on the TL spectrum to demonstrate the broadband sound insulation.

Figure 8(a) shows the TL spectra for channel widths varying from $a = 0.4$ cm to $a = 0.8$ cm. These system parameters are outside radius $R_2 = 5$ cm, inner radius $R_1 = 3.4$ cm, channel period $d = 1.57$ cm, wall thickness

$t = 0.1$ cm, the number of channels $N = 20$, structured period $l = 20$, and incident angle $\phi = 0°$. The simulation method is the same as described previously, and a weak contribution is included to implement the BLI condition in COMSOL Multiphysics. There are seven TL peaks presented in the TL spectrum for channel width $a = 0.4$ cm. However, with increasing channel width, the TL peaks show a blue shift because the channel length shortens, and the TL peaks broaden to form a broadband response (the TL values exceed 10 dB), shown as the white regions in Fig. 8(a). There are two special points to note in Fig. 8(a). Firstly, the TL peak with lowest frequency in the TL spectrum comes from the quadrupole resonant mode, as discussed in Fig. S3 of the Supplement Material [31], which gradually emerges and strengthens with increasing channel width. Secondly, a dip emerges in the TL spectra corresponding to the Wood's anomalies at 1.725 kHz, which depends on the period l of acoustic barrier. Thus, we can see that the dip is stationary for varying channel lengths rather than period l. To show the detail of the broadband sound insulation, we consider the TL spectrum of $a = 0.6$ cm in Fig. 8(b). It is not difficult to see that the TL values exceed 10 dB in the range of 1.655–2.05 kHz. This result means that the acoustic barrier can effectively block more than 90% of incident energy in the bandwidth of 395 Hz for a channel with width $a = 0.6$ cm. Four locations marked by red dots $D1$, $D2$, $D3$, and $D4$ in Fig. 8(a) correspond to the frequencies $f = 1.395$, 1.67, 1.865, and 1.96 kHz, respectively. Figures 8(c)–8(f) show the pressure field distributions for the locations $D1$, $D2$, $D3$, and $D4$. From the spatial field distributions, we can see that the incident waves are effectively blocked by the acoustic barrier.

V. EXPERIMENTAL DEMONSTRATION OF BROADBAND SOUND INSULATION

Next, we experimentally demonstrate the broadband sound insulation based on the aforementioned acoustic barrier. We perform a 2D experiment to measure the TL
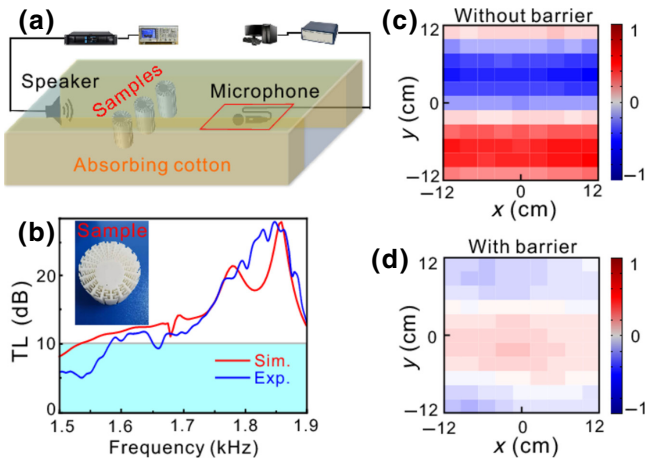
FIG. 9. (a) Schematic diagram of the experimental setup. (b) Transmission loss spectra of acoustic barrier obtained from numerical simulation (red line) and experimental measurements (blue line). The inset is the photograph of the physical sample. (c) and (d) represent pressure field distributions measured in the region marked by red solid box in (a) corresponding to without and with barrier, respectively.

spectrum and pressure field distributions, as shown in Fig. 9. Figure 9(a) shows the schematic diagram of the experimental setup, in which two acrylic plates are used to sandwich the samples to simulate the 2D scenario. The two faint yellow regions represent absorbing cotton as perfect matching layers. A loudspeaker, which receives signals from a signal generator (AFG1022, Tektronix) amplified by a power amplifier (CPA2400, SinoCinetech), launches incident waves from the left port of the waveguide. The magnitudes of the pressure fields behind the acoustic barriers are measured by a microphone (378B02, PCB Piezotronics). The experimental samples are fabricated by 3D printing technology: the structure (outside radius $R_2 = 5$ cm, initial inner radius $R_1 = 3.4$ cm, width of zigzag channel $a = 0.55$ cm, channel period $d = 1.57$ cm, gradient factor $\alpha = 0.35$) has 20 zigzag grooves, as shown in the inset of Fig. 9(b). The center to center spacing of the structures placed in the waveguide is 20 cm.

Figure 9(b) shows the TL spectra obtained from numerical simulation (red line) and experimental measurement (blue line). The experimental result indicates that the TL value of the acoustic barrier can exceed 10 dB for frequencies greater than 1.6 kHz. It is obvious that the discrete, distinct peaks fade and broaden to form broadband sound insulation (TL value exceeds 10 dB) due to the increased viscosity and heat losses in the practical measurements. The numerical calculation using the thermoviscous acoustic module of COMSOL Multiphysics, marked by the red line, is almost in agreement with the experimental result. Two distinct TL peaks located at high frequencies mainly come from the grooves with shallower depths due to smaller losses. To obtain a more direct display of sound

insulation, we also measure the pressure field distributions at a frequency of 1.6 kHz in the 24 cm × 24 cm region indicated by the red solid box of Fig. 9(a) without and with the acoustic barrier, as shown in Figs. 9(c) and 9(d), respectively. Comparing the pressure field distributions, it is not difficult to see that the acoustic barrier can effectively block the sound propagation at the frequency $f = 1.6$ kHz. From the TL spectrum in Fig. 9(b), we can see that the performance of the sound insulation will improve for high frequencies in the region from 1.6 kHz to 1.9 kHz. It is notable that the dips located at 1.66 kHz (experimental result) and 1.68 kHz (simulated result) come from the Wood's anomalies as discussed in Sec. III.

VI. CONCLUSION

In summary, we theoretically propose a closed surface consisting of radial gradient grooves to achieve a localized acoustic rainbow trapping effect, and demonstrate that the SASWs with different frequencies can be effectively trapped into different grooves. In particular, the trapped locations can be expediently tuned by changing the structural parameters. By means of the advantages of multiband responses and subwavelength scale of the closed surface, we design an acoustic barrier consisting of an array of structures to realize effective sound insulation with high ventilation. The numerical simulations verify the theoretical prediction that the acoustic barrier can block 90% of incident energy coming from various angles at multiple frequencies, even when considering the viscous and thermal losses. Finally, we discuss the influence of the zigzag channel width on the magnitude and bandwidth of the TL spectrum. The experimental results agree well with the theoretical predictions that the increase in channel width can broaden the TL peaks and form broadband sound insulation effects. These investigated results may have potential applications in acoustic energy collection, noise control, and sound processing.

[1] Q. Gan, Z. Fu, Y. J. Ding, and F. J. Bartoli, Ultrawidebandwidth Slow-Light System Based on THz Plasmonic Graded Metallic Grating Structures, Phys. Rev. Lett. **100,** 256803 (2008).

[2] Q. Gan, Y. J. Ding, and F. J. Bartoli, "Rainbow" Trapping and Releasing at Telecommunication Wavelengths, Phys. Rev. Lett. **102**, 056801 (2009).

[3] K. L. Tsakmakidis, A. D. Boardman, and O. Hess, 'Trapped rainbow' storage of light in metamaterials, Nature **450**, 397 (2007).

[4] Q. Hu, J.-Z. Zhao, R.-W. Peng, F. Gao, R.-L. Zhang, and M. Wang, "Rainbow" trapped in a self-similar coaxial optical waveguide, Appl. Phys. Lett. **96**, 161101 (2010).

[5] J. Park, K.-Y. Kim, I.-M. Lee, H. Na, S.-Y. Lee, and B. Lee, Trapping light in plasmonic waveguides, Opt. Express **18**, 598 (2010).

[6] M. S. Jang and H. Atwater, Plasmonic Rainbow Trapping Structures for Light Localization and Spectrum Splitting, Phys. Rev. Lett. **107**, 207401 (2011).

[7] Y. Cui, K. H. Fung, J. Xu, H. Ma, Y. Jin, S. He, and N. X. Fang, Ultrabroadband light absorption by a sawtooth anisotropic metamaterial slab, Nano Lett. **12**, 1443 (2012).

[8] V. Laude, J.-C. Beugnot, S. Benchabane, Y. Pennec, B. Djafari-Rouhani, N. Papanikolaou, J. M. Escalante, and A. Martinez, Simultaneous guidance of slow photons and slow acoustic phonons in silicon phoxonic crystal slabs, Opt. Express **19**, 9690 (2011).

[9] W. M. Robertson, C. Baker, and C. B. Bennett, Slow group velocity propagation of sound via defect coupling in a one-dimensional acoustic band gap array, Am. J. Phys. **72**, 255 (2004).

[10] J. Zhu, Y. Chen, X. Zhu, F. J. Garcia-Vidal, X. Yin, W. Zhang, and X. Zhang, Acoustic rainbow trapping, Sci. Rep. **3**, 1728 (2013).

[11] Y. Chen, H. Liu, M. Reilly, H. Bae, and M. Yu, Enhanced acoustic sensing through wave compression and pressure amplification in anisotropic metamaterials, Nat. Commun. **5**, 5247 (2014).

[12] X. Ni, Y. Wu, Z.-G. Chen, L.-Y. Zheng, Y.-L. Xu, P. Nayar, X.-P. Liu, M.-H. Lu, and Y.-F. Chen, Acoustic rainbow trapping by coiling up space, Sci. Rep. **4**, 7038 (2014).

[13] C. Zhou, B. Yuan, Y. Cheng, and X. Liu, Precise rainbow trapping for low-frequency acoustic waves with micro Mie resonance-based structures, Appl. Phys. Lett. **108**, 063501 (2016).

[14] J. Kang and M. W. Brocklesby, Feasibility of applying micro-perforated absorbers in acoustic window systems, Appl. Acoust. **66**, 669 (2005).

[15] X. Yu, S. K. Lau, L. Cheng, and F. Cui, A numerical investigation on the sound insulation of ventilation windows, Appl. Acoust. **117**, 113 (2017).

[16] N. Yuya, N. Sohei, N. Tsuyoshi, and Y. Takashi, Sound propagation in soundproofing casement windows, Appl. Acoust. **70**, 1160 (2009).

[17] S. Kumar and H. P. Lee, Recent advances in acoustic metamaterials for simultaneous sound attenuation and air ventilation performances, Crystals **10**, 686 (2020).

[18] S.-H. Kim and S.-H. Lee, Air transparent soundproof window, AIP Adv. **4**, 117123 (2014).

[19] Z. Yang, H. M. Dai, N. H. Chan, G. C. Ma, and P. Sheng, Acoustic metamaterial panels for sound attenuation in the 50–1000 Hz regime, Appl. Phys. Lett. **96**, 041906 (2010).

[20] G. Ma, M. Yang, S. Xiao, Z. Yang, and P. Sheng, Acoustic metasurface with hybrid resonances, Nat. Mater. **13**, 873 (2014).

[21] Y. Cheng, C. Zhou, B. G. Yuan, D. J. Wu, Q. Wei, and X. J. Liu, Ultra-sparse metasurface for high reflection of low frequency sound based on artificial Mie resonances, Nat. Mater. **14**, 1013 (2015).

[22] X. Su and D. Banerjee, Extraordinary Sound Isolation Using an Ultrasparse Array of Degenerate Anisotropic Scatterers, Phys. Rev. Appl. **13**, 064047 (2020).

[23] C. Shen, Y. Xie, J. Li, S. A. Cummer, and Y. Jing, Acoustic metacages for sound shielding with steady air flow, J. Appl. Phys. **123**, 124501 (2018).

[24] X. Wu, K. Y. Au-Yeung, X. Li, R. C. Roberts, J. Tian, C. Hu, Y. Huang, S. Wang, Z. Yang, and W. Wen, High-efficiency ventilated metamaterial absorber at low frequency, Appl. Phys. Lett. **112**, 103505 (2018).

[25] H. L. Zhang, Y. F. Zhu, B. Liang, J. Yang, J. Yang, and J. C. Cheng, Omnidirectional ventilated acoustic barrier, Appl. Phys. Lett. **111**, 203502 (2017).

[26] R. Ghaffarivardavagh, J. Nikolajczyk, S. Anderson, and X. Zhang, Ultra-open acoustic metamaterial silencer based on fano-like interference, Phys. Rev. B **99**, 024302 (2019).

[27] L. J. Li, B. Zheng, L. M. Zhong, J. Yang, B. Liang, and J. C. Cheng, Broadband compact acoustic absorber with high efficiency ventilation performance, Appl. Phys. Lett. **113**, 103501 (2018).

[28] M. Sun, X. S. Fang, D. X. Mao, X. Wang, and Y. Li, Broadband Acoustic Ventilation Barriers, Phys. Rev. Appl. **13**, 044028 (2020).

[29] YG,H Sun, S. Yuan, and Y. Lai, Switchable omnidirectional acoustic insulation through open window structures with ultrathin metasurfaces, Phys. Rev. Mater. **3**, 065203 (2019).

[30] X. Zhu, B. Liang, W. Kan, Y. Peng, and J. Cheng, Deep-subwavelength-scale Directional Sensing Based on Highly Localized Dipolar Mie Resonances, Phys. Rev. Appl. **5**, 054015 (2016).

[31] See Supplement Material at http://link.aps.org/supplemental/10.1103/PhysRevApplied.15.054033 for the equivalent material parameters of the metafluid in grooves, equivalent material parameters of the closed surface based on the homogenized metamaterial approximation, localized resonant mode distributions, which includes Refs. [30, 32].

[32] F. Liu, W. Li, and M. Ke, Rigorous Analytical Model for Multipole Emission Enhancement Using Acoustic Metamaterials, Phys. Rev. Appl. **10**, 054031 (2018).

[33] R. W. Wood, On a remarkable case of uneven distribution of light in a diffraction grating spectrum, Philos. Mag. **4**, 396 (1902).

[34] D.-X. Qi, R.-H. Fan, R.-W. Peng, X.-R. Huang, M.-H. Lu, X. Ni, Q. Hu, and M. Wang, Multiple-band transmission of acoustic wave through metallic gratings, Appl. Phys. Lett. **101**, 061912 (2012).